Computers and Concrete, *Vol. 20, No. 6 (2017) 689-704*
DOI: https://doi.org/10.12989/cac.2017.20.6.689

Experiments and numerical analyses for composite RC-EPS slabs

Ł. Skarżyński[a], I. Marzec[a] and J. Tejchman*

Faculty of Civil and Environmental Engineering, Gdańsk University of Technology, Narutowicza 11/12, 80-233 Gdańsk, Poland

(Received January 28, 2016, Revised July 26, 2017, Accepted August 10, 2017)

Abstract. The paper presents experimental and numerical investigations of prefabricated composite structural building reinforced concrete slabs with the insulating material for a residential building construction. The building slabs were composed of concrete and expanded polystyrene. In experiments, the slabs in the full-scale 1:1 were subjected to vertical concentrated loads and failed along a diagonal shear crack. The experiments were numerically evaluated using the finite element method based on two different constitutive continuum models for concrete. First, an elasto-plastic model with the Drucker-Prager criterion defined in compression and with the Rankine criterion defined in tension was used. Second, a coupled elasto-plastic-damage formulation based on the strain equivalence hypothesis was used. In order to describe strain localization in concrete, both models were enhanced in the softening regime by a characteristic length of micro-structure by means of a non-local theory. Attention was paid to the formation of critical diagonal shear crack which was a failure precursor.

Keywords: composite slabs; elasto-plasticity; damage mechanics; non-local theory; reinforced concrete; EPS foam; diagonal shear crack

1. Introduction

Nowadays, in order to diminish construction costs and to shorten construction time of residential buildings, different prefabricated systems are offered on the building market. Prefabricated building is a type of building that consists of several factory-built components or units that are assembled on-site to complete the unit. In addition, the structural design can be improved through the development and application of composite elements. An attractive energy-saving construction system for residential buildings was proposed, composed of monolithic load bearing reinforced concrete (RC) frames and prefabricated composite slabs and wall panels composed of reinforced concrete (RC) and expanded polystyrene (EPS) (Sewaco System, www.sewaco.pl). The advantages of such a construction system are: a) short time of the building process due to presence of prefabrication for slabs and walls during a construction process (3 times shorter than a standard monolithic construction), b) energy-saving due to the presence of RC and EPS (thermal conductivity coefficient of external envelopes is only 0.11-0.15kW/m^{2}K), c) high apparent sound reduction index R due to the presence of reinforced concrete and EPS (R=33-34 dB) and d) high standard of finish.

The slabs were composed of RC ribbed box elements with the core from the (EPS) foam as a thermal insulation material. Both the materials (RC and EPS) were together constructed in a prefabrication factory. The slabs were 7.07 m long and 2.4 m wide with the total thickness of 0.30 m. The expanded polystyrene (EPS) foam core had the thickness of 0.23 m. In engineering design calculations of residential houses, it was assumed that all loads were carried by slabs supported on spatial monolithic longitudinal and transverse RC frames located on ground beams and footings. The slabs were dimensioned in the usual way as RC T-elements without EPS.

Our paper is experimentally and theoretically oriented. It focuses on studying the strength, deformability and failure of RC concrete slabs without shear reinforcement under 4-point bending, based on full-scale laboratory tests in order to evaluate their real strength. Such full-scale tests always provide the most valuable information on the behaviour of concrete elements (De Luca *et al.* 2014, Dulude *et al.* 2011, Lantsoght *et al.* 2010). The slabs failed along a diagonal shear crack. Initially the experimental results were compared with a theoretical formula for the shear capacity of RC-elements. Next, a numerical deterministic evaluation of experimental results using two different continuum constitutive models for concrete was conducted. First, an elasto-plastic model with a Drucker-Prager criterion defined in compression and with a Rankine criterion defined in tension was used. Second, a coupled elasto-plastic-damage formulation based on the strain equivalence hypothesis was used. The latter is obviously a more physical constitutive model for describing a non-linear concrete behaviour in tension. However, the elasto-plastic models are still frequently used for concrete modelling due to its simplicity. Therefore, these two different formulations were used for solving the same problem. In order to ensure mesh-independent FE results and to properly describe strain localization in concrete, both models were enhanced in the softening regime by a characteristic length of micro-structure by means of a non-

*Corresponding author, Professor
E-mail: tejchmk@pg.gda.pl
[a]Ph.D.

http://www.techno-press.org/?journal=cac&subpage=8 ISSN: 1598-8198 (Print), 1598-818X (Online)

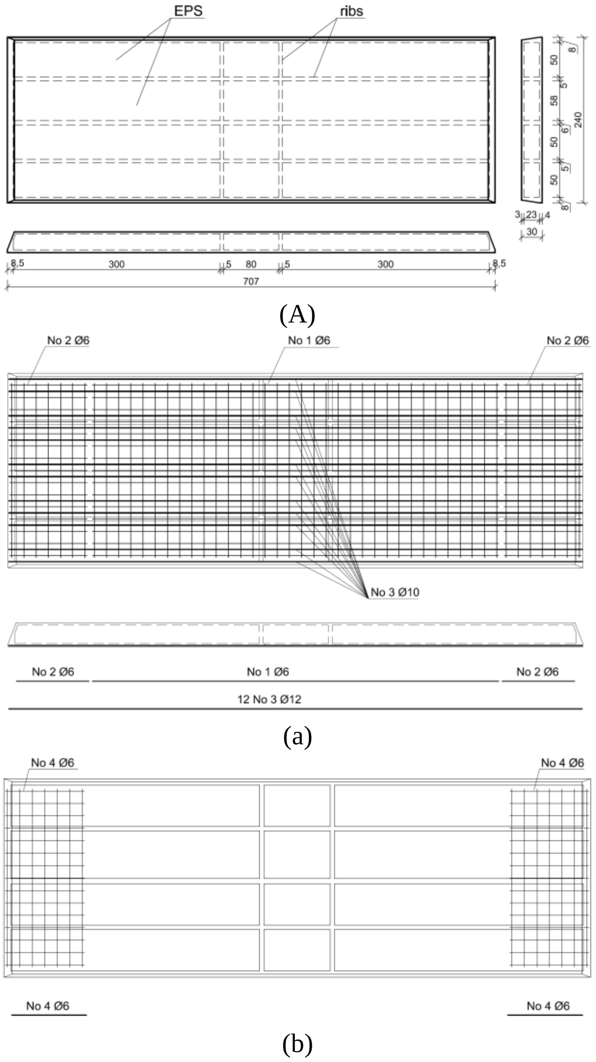

Fig. 1 Composite slab (length L=7.01 m, width b=2.4 m and thickness h=0.30 m): (A) geometry and (B) reinforcement in form of single bars and bar mesh (a) top and (b) bottom)

local theory. For simulations of the reinforcement behaviour, an associated elasto-perfectly plastic constitutive law was assumed. EPS was described by a linear elastic model. Attention was paid to a critical diagonal crack which developed before the maximum vertical load was reached. This diagonal crack plays an important role in the shear brittle failure of typical RC beams under concentrated vertical loads and is responsible for a deterministic size effect due to concrete failure (Syroka-Korol and Tejchman 2014, Korol *et al.* 2014). A statistical size effect is negligible in this case since the location of a critical is always similar independently of the beam size (Korol *et al.* 2014).

The innovative points in this paper are twofold (beneficial for the optimum engineering design): a) experimental investigations of large novel composite building slabs in the scale 1:1 under bending and b) validation of two different continuum approaches for concrete in order to describe the shear strength, deflection and pattern of shear and bending localization zones in large RC elements (by taking bond-slip into account). The

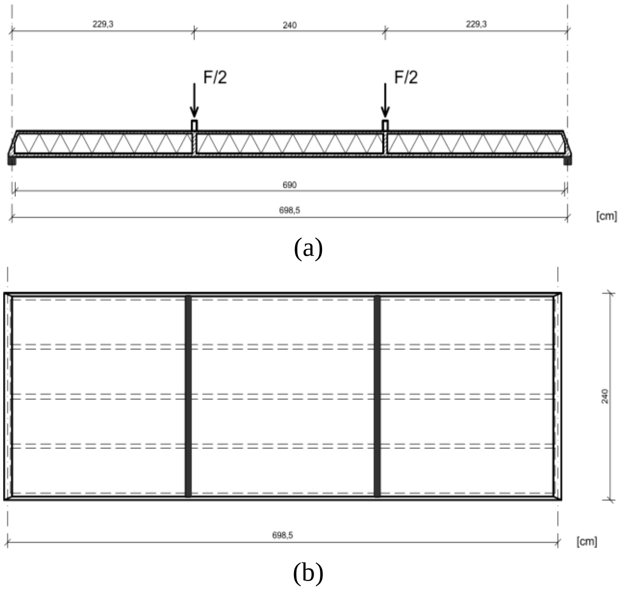

Fig. 2 Loading system of composite slab during four-point bending with steel profiles transmitting loads: (a) side view and (b) top view (dimensions in (cm))

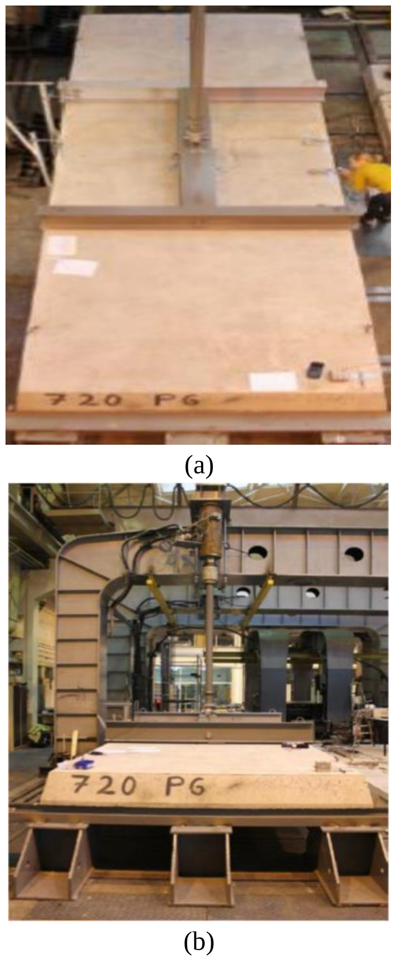

Fig. 3 Experimental set-up for composite slab: (a) top view and (b) side view

experimental and numerical results concerning composite wall panels under the vertical load will be published later.

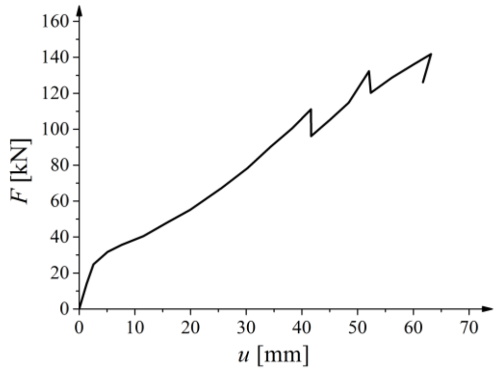

Fig. 4 Evolution of experimental vertical force F against mid-slab deflection u in composite slab (two zig-zags on curve were caused by technical reasons-two stop-restart processes)

(a)

(b)

(c)

(d)

Fig. 5 Crack pattern evolution (in red) in composite slab for the vertical force F: (a) for 25% of failure force F_{max}, (b) for 40% of F_{max}, (c) for 60% of F_{max} and (d) at failure (note that cracks in red are shown for slab at failure)

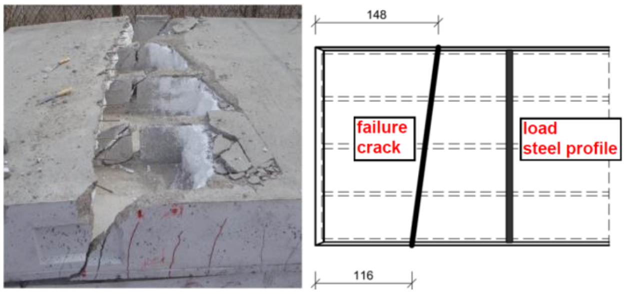

(a)

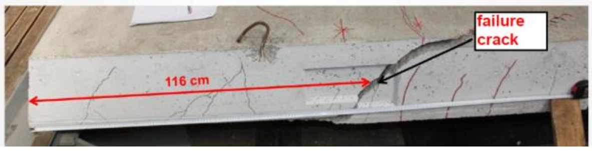

(b)

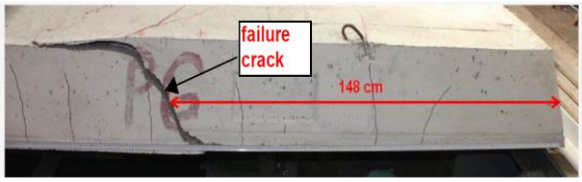

(c)

Fig. 6 Failure crack location in composite slab: (a) view from top (note damaged internal ribs), (b) left side view and (c) right side view

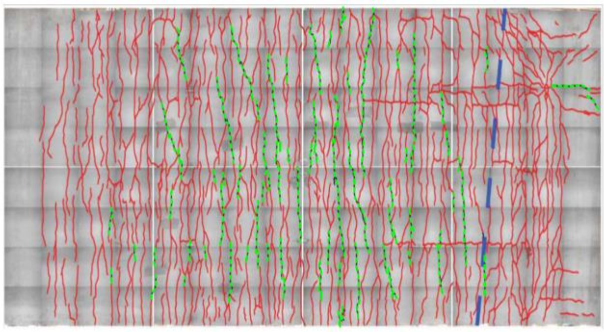

Fig. 7 Crack pattern on bottom surface of composite slab (Green lines-initial cracks due to transportation, red lines-cracks before failure, blue dotted line-critical diagonal shear crack)

2. Laboratory full-scale tests on composite slabs

The geometry of the composite slab is shown in Fig. 1. The RC slab was made in a usual prefabrication factory. It had a thin-walled box-type cross-section filled with EPS. Five ribs were used in the longitudinal direction and two in the transverse direction. The concrete was prepared from the ordinary Portland cement (CEM I 42.5 R), aggregate and water. The river sand and gravel aggregate were used with the mean particle diameter d_{50}=2 mm, maximum aggregate diameter d_{max}=8 mm and aggregate volume of 75%. The water to cement ratio was equal to 0.42. The reinforcement ratio of the main lower horizontal reinforcement was 0.6% (13 bars ϕ10 and 15 bars ϕ6) and main upper longitudinal reinforcement ratio was 0.2% (30 bars ϕ6 located in the support neighbourhood). The horizontal bars with the diameter of 10 mm and bar meshes with the diameter of 6 mm were used at the distance of 150 mm in the both direction. The concrete cover measured from the bar centre to the concrete surface was 20 mm (bottom) and 15 mm (top). The average cylinder compressive strength of concrete was f_{cm}=40.5 MPa and the average cylinder splitting tensile strength of concrete was f_{ctm}=2.06 MPa. The average modulus of elasticity of concrete was E_c=30.3 GPa. The yield strength of reinforcement was about f_y=600 MPa and its modulus of elasticity was E_s=200 GPa.

Two slabs were incrementally loaded by 2 vertical band forces applied through two steel I-beams placed at the mid-span of each slab at the distance of 2.4 m (Fig. 2) and at the distance of a=2.22 m (a/h=7) from the supports. In the test, the span was equal to 6.9 m and slab was free at the ends. The supports had the width of 85 mm. In order to avoid local damage of concrete surface, rubber pads were placed between steel profiles and concrete surface. The quasi-static

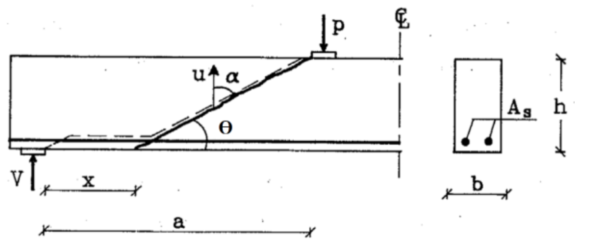

Fig. 8 Shear failure mechanism of RC beam with cross-section $b\times h$ in plastic theory by Nielsen and Bræstrup (1976)

tests were performed with the controlled displacement rate of 7 mm/h. The initial maximum deflection (caused by its weight) of slabs was about 7-9 mm. The slabs had some initial transverse bending cracks with the width in the range of 0.10-0.15 mm due to a too fast lifting for transportation purposes (see Fig. 7). During the experiments, the following quantities were measured: vertical force, deflection at the mid-span and under the forces using induction gauges, normal tensile stress in lower reinforcement bars at the mid-span using electric strain gauges (2 points), normal compression stress in concrete at the mid-span using electric strain gauges (2 points), angle of rotation of supports using an inclinometer (2 points) and width of cracks using induction gauges and manual measurements. We used the strain gauges (produced by the Tenmex company) with the length of 20 mm and width of 5 mm. Their measurement accuracy was 0.0005. The experimental set-up is presented in Fig. 3.

Figs. 4-7 show the typical experimental force-deflection curve F=f(u) after loading and crack pattern for one slab under 4-point bending. The maximum vertical failure force was $F_{\max}$=142.3 kN (Fig. 4). With the slab weight, the failure force was $F_{\max}$=184.3 kN. For 0.25$F_{\max}$, some bending cracks first appeared in the slab mid-span (Fig. 5). The first bending crack with the width of 0.3 mm appeared for F=51.4 kN and u=17.6 mm (Fig. 5). Then, for about 0.6F_{max} (F=85 kN) and u=37.5 mm, the first inclined shear crack occurred. When the vertical force was F=108 kN (75% of $F_{\max}$) and deflection was u=45.5 mm, the critical diagonal shear crack was 0.05 mm wide and propagated up to the half of the slab thickness. The slab took place in a rapid brittle way for $F_{\max}$=142.3 kN due to a diagonal shear crack moving through the beam compressive zone towards the loading point (Fig. 6). The pattern of vertical bending cracks was almost symmetric during almost the entire deformation process (Fig. 5). Their mean length along the beam height was l_c=0.19 m after the test. The maximum failure deflection was $u_{\max}$=63 mm ($F_{\max}$=142.3 kN). When considering the initial deflection due to the slab weight, the maximum deflection was $u_{\max}$=70.3 mm. Since the cracks did not appear at places of initial existing bending cracks due to transportation and the shear failure mode occurred, one might assume that the effect of initial cracks on experimental results was negligible. The uniform surface load used in usual standard dimensioning analyses (corresponding to the maximum experimental bending moment) was $q_{\max}$=10.67 kN/m^2

In the experiments the average spacing of vertical bending cracks varied during the deformation process. For F=35 kN their average spacing was s=343 mm. Afterwards, for F=55 kN more vertical cracks appeared and their average spacing was s=200 mm. For F=82 kN, additional vertical cracks appeared (s=171 mm). At the failure the average crack spacing was s=145 mm. A failure diagonal shear crack appeared in the slab. It was surprisingly strongly non-symmetric. Its distance from the slab end was along the horizontal mid-thickness line was x_1=116 cm (slab right side) and x_2=148 cm (slab left side) (Figs. 6 and 7) (the mean distance was thus $\bar{x}$=132 cm > a/2=111 cm). Its distance along the slab bottom line was x_1=100 cm (right side) and x_2=128 cm (left side) (Fig. 6) ($\bar{x}$=114 cm > a/2=111 cm). Its inclination to the horizontal was different at the both slab sides: β_l=38° (left side) and β_r=53° (right side) on average (the mean value along the slab width was $\bar{\beta}$=45.5°) (Fig. 6). The failure diagonal crack crossed all slab ribs (Fig. 6). The maximum failure shear crack width was 0.57 mm. At the failure, the measured maximum normal tensile stress in the reinforcement at the mid-span was 614 MPa$\approx f_y$ (but it has not yielded yet) and the measured maximum compressive stress in concrete at the mid-span was 14.85 MPa ($\ll f_{cm}$=40.5 MPa). The maximum angle of the support rotation was negligible (1.48°).

3. Analytical calculations

Initially, the shear strength of the slab was analytically calculated as RC beams with a rectangular cross-section without shear reinforcement (Nielsen and Bræstrup 1976, Zhang 1994). In the modified plasticity theory, one assumed that the critical diagonal shear crack developed at the distance of x from the support (Fig. 8). The beam shear strength (the upper bound solution) based on the equality of the external energy and internal work dissipated along the crack was

$$\upsilon = 0.5\upsilon_0\upsilon_s f_{ck}\left[\sqrt{1+\left(\frac{a-x}{D}\right)^2}-\frac{a-x}{D}\right] \qquad (1)$$

with x=0.74D(a/D-2),

wherein υ=V/($b\times D$), V-the maximum shear force, b-the beam width, D-the effective beam height, a-the distance of the vertical force from the support, x-the distance of the critical diagonal shear crack from the support along the bottom and $\upsilon_0\times\upsilon_s\times f_{ck}$ denotes the effective concrete shear strength which considers the concrete cohesion reduction factor due to micro-cracking υ_o and sliding reduction factor due to cracking υ_s. The experimental and theoretical results were compared in Tab.1. In the theoretical calculations, the following values were assumed: υ_0=0.7, υ_s=0.67 (Nielsen and Bræstrup 1976) or υ_s=0.5 (Zhang 1994), f_{ck}=f_{cm}=40.5MPa, a=2.22 m and D=0.28 m. The inclination of the critical diagonal shear crack with respect to the bottom edge was θ=15.7° (tanθ =D/(a-x)=0.28/0.99=0.28 with x=1.23 m) and was strongly smaller than the mean experimental value $\bar{\theta}$ =45.5°. The theoretical shear strength, υ=1234.6 kPa (υ_s=0.67) or υ=921.4 kPa (υ_s=0.5), was lower by 7% and 40% than the experimental one (υ=1328 kPa). The calculated distance of the critical diagonal shear crack from the support along the bottom line, x=1.23 m, was higher by about 10% than the mean experimental distance ($\bar{x}$ =1.14 m). The main disadvantage of the formula is the fact that the shear strength constants υ_o and υ_s are in general non-linear and depend on many different factors (Nielsen and Bræstrup 1976, Zhang 1994).

The standard permissible bending moment M_{Rd} and shear force V_{Rd} were calculated for the slab according to the Polish Standard (2002) with the real strength parameters of concrete and steel. The total standard (with load factors) vertical uniform surface load on the slab (including the slab dead weight, weight of finishing layers and live load) was q_d=7.86 kN/m^2 and the total characteristic (without load factors) value was q=6.31 kN/m^2. Both the standard quantities V_{Rd}=102.3 kN and M_{Rd}=218.1 kNm were higher than the experimental outcomes (V_{max}=0.5F_{max}=92.3 kN and M_{max}=V×a=204.9 kNm). The experimental slab strength, expressed by the maximum vertical uniform surface load of q_{max}=10.65 kN/m^2, indicated that the slab had the greater shear strength by 30% than the standard load of q_d=7.86kN/m^2. The comparisons with the standard requirements PN-B-03264 (2002) with respect to the permissible both crack width and deflection were carried out by taking into account initial bending cracks due to transportation. The standard crack width requirement of 0.3 mm was satisfied since the total permissible uniform surface load was larger than 9.36 kN/m^2. The deflection requirement of 30 mm was however exceeded by 2%. Therefore, it was recommended to slightly decrease the slab deflection by increasing the longitudinal bottom reinforcement area (13 bars ϕ12 and 15 bars ϕ6 instead of 13 bars ϕ10 and 15 bars ϕ6). In addition, the bottom slab should be connected with the longitudinal ribs by the L-bars ϕ6 at the distance of 0.15 m to enhance the shear strength of the element in weaken places.

The experimental spacing of vertical bending cracks was compared with the average crack spacing according to CEB-FIP Model Code (1991)

$$s=\frac{2}{3}+\frac{\phi_s}{3.6\rho}=\frac{2}{3}\times\frac{8}{3.6\times 0.006}=247\,\text{mm}, \tag{2}$$

the formula by Lorrain *et al.* (1998)

$$s=1.5c+0.1\frac{\phi_s}{\rho}=1.5\times 20+0.1\frac{8}{0.006}=163\text{ mm}, \tag{3}$$

and according to Eurocode 2 (1992)

$$s=3.4c+0.425\frac{k_1k_2\phi_{eq}}{\rho_{p,eff}}=3.4\times 20+0.425\frac{0.8\times 0.5\times 8.3}{0.0183}=145\text{ mm} \tag{4}$$

wherein $\o_s$=8 mm is the mean bar diameter, ρ=0.6% denotes the horizontal reinforcement ratio, c=20 mm denotes the concrete cover, $\o_{eq}$=8.3 mm is the equivalent bar diameter, $\rho_{p,eff}$=1.83% denotes the horizontal reinforcement ratio in the effective tension area, c=20 mm is the concrete cover and k_1 and k_2 are coefficients which take into account the bond properties of reinforcement and strain distribution. The mean experimental spacing of main vertical cracks, 145 mm, was similar to this according to Eq. (4) (s=145 mm), smaller by 15% than this according to Eq. (3) (s=163 mm) and smaller by 70% than this according to Eq. (2) (s=247 mm).

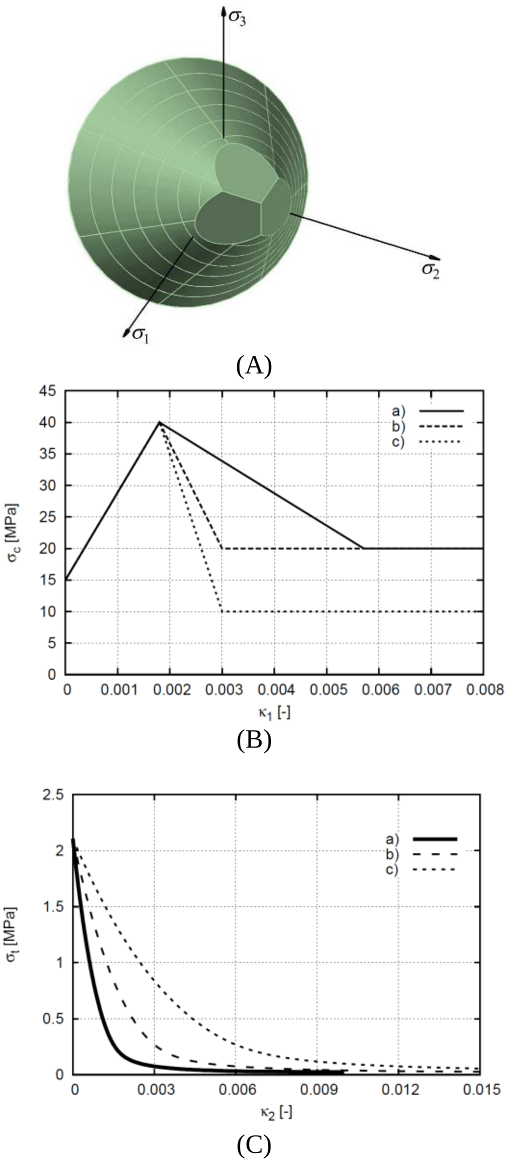

Fig. 9 Coupled Drucker-Prager-Rankine criterion for concrete in space of principal stresses (A) and different curves in enhanced elasto-plasticity: (B) hardening/softening curve σ_c=f(κ_1) in compressive regime (a) G_c=4000 N/m, (b) G_c=3250 N/m, (c) G_c=2500 N/m), (C) softening curve σ_t=f(κ_2) in tensile regime (a) G_f=100 N/m, (b) G_f=200 N/m, (c) G_f=400 N/m): (σ_c-compressive stress, σ_t-tensile stress, κ_i-hardening/softening parameter)

4. Constitutive models for concrete, reinforcement and EPS

Elasto-plastic model for concrete

Two different constitutive models for concrete were used: an isotropic elasto-plastic model (Eqs. (A1)-(A6),

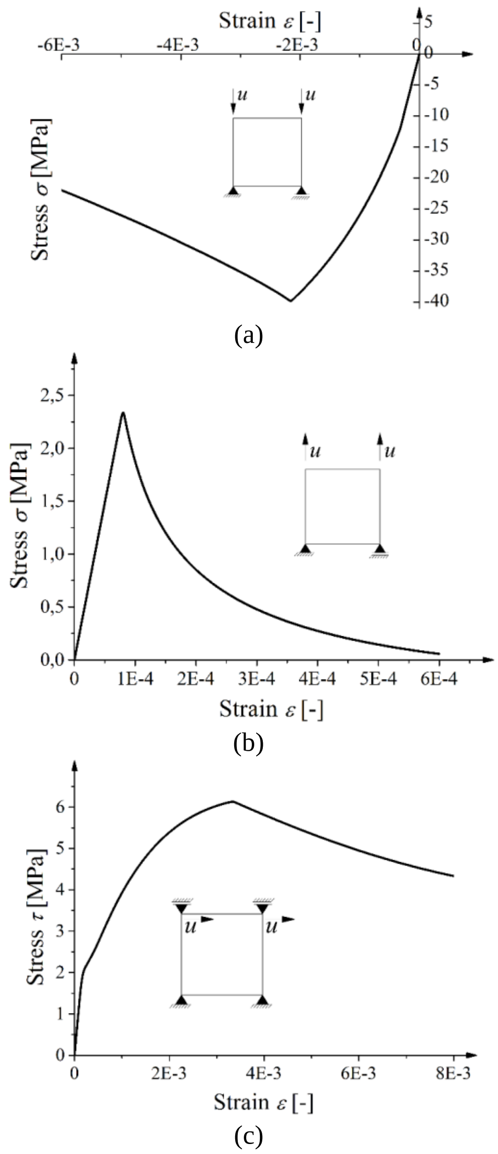

Fig. 10 Element tests for concrete response (within elasto-plastic-damage): (a) uniaxial compression, (b) uniaxial tension and (c) simple shear

Appendix 1) and a coupled elasto-plastic-damage model (Eqs. (A7)-(A14), Appendix 2).

Elasto-plastic models have been widely used to describe concrete behaviour in compression, tension and shear (e.g., Willam and Warnke 1975, Etse and Willam 1994, Feenstra and De Borst 1996). Our isotropic elasto-plastic model for concrete (Marzec *et al.* 2007, Majewski *et al*. 2008, Tejchman and Bobiński 2012, Korol *et al.* 2014) includes the Drucker-Prager criterion (defined in compression) and the Rankine criterion (defined in tension) (Fig. 9(A)). It requires two elastic parameters: modulus of elasticity E and Poisson's ratio υ, one compression yield stress function $\sigma_c=f(\kappa_1)$ (based on uniaxial compression tests), one tensile yield stress function $\sigma_t=f(\kappa_2)$ (based on uniaxial tension tests), internal friction angle φ and dilatancy angle ψ based on a triaxial compression test (Gabet *et al.* 2008). The constitutive model has some disadvantages as e.g., the shape of the failure surface in the principal stress space is conical (not paraboloidal as in reality). In addition, in deviatoric planes, the shape is circular (during compression) and triangular (during tension); thus, it does not gradually change from a curvilinear triangle with smoothly rounded corners to nearly circular with increasing pressure. In our elasto-plastic model, the stiffness degradation due to strain localization (damage zones) and non-linear volume changes during loading are not taken into account.

The following material parameters were assumed in FE simulations: E=30.3 GPa, υ=0.20, f_c=40.5 MPa (compressive strength) and f_t=2.06 MPa (tensile strength), based on laboratory experimental outcomes. The assumed relationship between the compressive stress σ_c and hardening (softening) parameter κ_1 was composed of 3 linear parts. One assumed 3 different relationships (Fig.9(B)). The compressive fracture energy G_c varied between 2500-4000 N/m. It was calculated as $G_c=g_c\times w_c$ (g_c-area under the entire softening/hardening function up to κ_1=0.006, $w_c\approx 3.5\times l_c$-the width of compressive localization zones, l_c=5 mm, Section 5). In the case of the tensile fracture energy 2 different exponential Hordijk (2011) curves wereanalysed (Fig. 9(c)). The tensile fracture energy G_f varied between 100-400 N/m. It was calculated as $G_f=g_f\times w_f$ (g_f-area under the entire softening function, $w_f\approx 3.5\times l_c$-width of tensile localization zones, l_c=5 mm, Section 5). The internal friction angle was equal φ=12° (Eq.(2)), dilatancy angle ψ=8° (Abaqus 2004) and non-locality parameter m=2 (Brinkgreve 1994).

Coupled elasto-plastic damage model for concrete

Besides elasto-plastic formulations to the describe the concrete behaviour under monotonic loading, damage (Krajcinovic and Fonseka 1981, Mazars 1986) and coupled elasto-plastic damage formulations (Lubliner *et al.* 1989, Meschke *et al.* 1998, Faria *et al.* 1998) also may also be used. The constitutive model (Marzec and Tejchman 2012, Tejchman and Bobiński 2012, Marzec *et al.* 2013, Korol *et al*. 2017) combines elasto-plasticity with damage mechanics. It assumes the different stiffness in tension and compression and a positive-negative stress projection operator to simulate crack closing and crack re-opening. It shares main properties of the model by Lee and Fenves (1998) which was proved to not violate thermodynamic principles, expressed by the lack of the spurious energy dissipation, Carol and Willam (1996), since plasticity was defined in the effective stress space, isotropic damage was used and the stress weight function was continuous. Carol and Willam (1996) showed namely that for damage models with crack-closing-re-opening effects, only isotropic formulations did not suffer from spurious energy dissipation under non-proportional loading in contrast to anisotropic ones. Similar coupled models were presented for concrete by Simo and Ju (1997) and more recently by Chen *et al*. (2012), Grassl *et al.* (2013), Mihai e*t al.* (2016) and Xotta *et al.* (2016).

The coupled elasto-plastic-damage model requires the following 12 material constants E, υ, κ_0, α, β, η_1, η_2, δ, a_t, a_c, ψ and φ and 2 hardening yield stress functions (the Rankine function in tension and the Drucker-Prager function in compression). In the case of linear hardening, 16 material constants are needed (E, υ, κ_0, α, β, η_1, η_2, δ, a_t, a_c, ψ, φ, initial yield stresses σ_{yt}^0 (tension) and σ_{yc}^0 (compression) and plastic hardening moduli H_p (in compression and in tension). If the tensile failure prevails, one yield stress function by Rankine can be used. The quantities σ_y^0 (initial yield stress during hardening) and κ_0 are responsible for the peak location on the stress-strain curve and a simultaneous activation of the plasticity and damage criteria (usually the initial yield stress in the hardening function σ_{yt}^0=3.5-6.0 MPa and κ_0=(8-15)×10^{-5} under tension). The shape of the stress-strain-curve in softening is influenced by the constant β in tension (usually β=50-800), and by the constants δ and η_2 in compression (usually δ=50-800 and η_2=0.1-0.8). The parameter η_2 influences also the hardening curve in compression. In turn, the stress-strain curve at the residual state is affected by the constant α (usually α=0.70-0.95) in tension and by the constant η_1 in compression (usually η_1=1.0-1.2). Since the parameters α and η_1 are solely influenced by high values of κ, they can arbitrarily be assumed for softening materials. Thus, the most crucial material constants are σ_y^0, κ_0, β, δ and η_2. In turn, the scale factors a_t and a_c influence the damage magnitude in tension and compression. In general, they vary between zero and one. There do not exist unfortunately experimental data allowing for determining the values of a_t and a_c. Since, the compressive stiffness is recovered upon the crack closure as the load changes from tension to compression and the tensile stiffness is not recovered due to compressive micro-cracks, the parameters a_c and a_t can be taken for the sake of simplicity as a_c=1.0 and a_t=0 for many different simple loading cases as e.g., uniaxial tension and bending. The equivalent strain measure $\tilde{\varepsilon}$ was defined in terms of elastic strains. In uniaxial compression, the material strength increased with increasing κ_0 and decreasing δ and η_2 and the material ductility reduced with increasing both δ and η_2. The effect of β was negligible. In uniaxial tension, the material strength increased with growing κ_0 only. The material ductility mainly decreased with increasing β. The drawback of this formulation is the necessity to tune up constants controling plasticity and damage to activate an elasto-plastic criterion and a damage criterion at the same moment. As a consequence, the chosen initial yield stress σ_y^0 may be higher than this obtained directly in simple monotonic laboratory experiments. The material constants E, ν, κ_0, β, α, η_1, η_2, δ and two hardening yield stress functions should be determined for concrete by means of two independent full monotonic tests: uniaxial compression test and uniaxial tension (or three-point bending) test. However, the determination of the damage scale factors a_t and a_c requires one full cyclic compressive test and one full cyclic tensile (or three-point bending) test. In addition, the values of φ and ψ may be determined by means of triaxial compression tests. Due to the lack of laboratory stress-strain curves during uniaxial compression and uniaxial tension, a simplified calibration procedure of the constitutive model was performed for concrete. The material constants were fitted to the uniaxial compressive strength f_{cm}=40.5 MPa. Initially the following set of the material constants was assumed for FE calculations with the slab: E=30 GPa and ν=0.2 (measured values), σ_{yt}^0=3.5 MPa, σ_{yc}^0=40 MPa (compression), H_p=19 GPa, κ_0=8×10^{-5}, ϕ=14°, ψ=8°, β=100, α=0.90, η_1=1.05, η_2=0.30, δ=300, a_t=0, a_c=1. The value of ϕ=14° was calculated with Eq. (A5) and the value of ψ=8° was chosen based on our earlier calculations within elasto-plasticity (Tejchman and Bobiński 2012). Using the assumed material constants, the fracture energies were: G_f=130 N/m (in tension) and G_c=2550 N/m (in compression) and the uniaxial tensile strength was f_t=2.2MPa≈f_{ctm}. The concrete behaviour during element tests (uniaxial compression, uniaxial tension and shear) is shown in Fig. 10. In computations of slabs the other values of H_p and β were also assumed (H_p=7.5 GPa and β=300).

Non-local approach for concrete

A non-local theory was used as a regularization technique (Bažant and Jirásek 2002, Pijauder-Cabot and Bažant 1987, Bažant *et al.* 2010, Giry *et al.* 2011, Tejchman and Bobiński 2012, Bobiński and Tejchman 2016). In this approach, the principle of a local action does not hold any more. Polizzotto *et al.* (1998) and Borino *et al.* (2003) laid down a thermodynamically consistent formulation of non-local plasticity and non-local damage. In the calculations, the softening parameters κ_i (i=1, 2) were assumed to be non-local (independently for both yield surfaces f_i) (Brinkgreve 1994)

$$\bar{\kappa}_i(\boldsymbol{x}) = (1-m)\kappa_i(\boldsymbol{x}) + m\frac{\int_V \omega(\|\boldsymbol{x}-\boldsymbol{\xi}\|)\kappa_i(\boldsymbol{\xi})\mathrm{d}\boldsymbol{\xi}}{\int_V \omega(\|\boldsymbol{x}-\boldsymbol{\xi}\|)\mathrm{d}\boldsymbol{\xi}} \quad \text{for } =1, 2, \tag{5}$$

where $\bar{\kappa}_i\ (\boldsymbol{x})$ are the non-local softening parameters, V denotes the body volume, $\boldsymbol{x}$ is the coordinate vector of the considered point, $\boldsymbol{\xi}$ is the coordinate vector of the surrounding points, ω denotes the weighting function and m is the additional non-locality parameter also controlling, except of l_c, the size of a localization zone (Brinkgreve 1994, Bobiński and Tejchman 2004). In the calculations within and coupled elasto-plastic-damage, the equivalent strain measure $\tilde{\varepsilon}$ was replaced by its non-local definition (Pijauder-Cabot and Bažant 1987, Saouridis and Mazars 1992)

$$\bar{\varepsilon} = \frac{\int_V \omega(\|\boldsymbol{x}-\boldsymbol{\xi}\|)\tilde{\varepsilon}(\boldsymbol{\xi})\mathrm{d}\boldsymbol{\xi}}{\int_V \omega(\|\boldsymbol{x}-\boldsymbol{\xi}\|)\mathrm{d}\boldsymbol{\xi}}. \tag{6}$$

As a weighting function ω, the Gauss distribution function was used (Bažant and Jirásek 2002)

$$\omega(r) = \frac{1}{l_c\sqrt{\pi}} e^{-\left(\frac{r}{l_c}\right)^2}, \tag{7}$$

where l_c is a characteristic length of micro-structure and the parameter r denotes the distance between material points. The averaging in Eq. (5) was restricted to a small representative area around each material point (the influence of points at the distance of r=3×l_c was only of 0.01%). The characteristic length is mainly determined with an inverse identification process of experimental data (Mahnken and Kuhl 1999, Skarżyński *et al.* 2011). In order to simplify the calculations, non-local rates were replaced by their approximations calculated with known total strain increments (Brinkgreve 1994). The characteristic length l_c of micro-structure within isotropic elasto-plasticity and isotropic damage mechanics may be about 2 mm (fine-grained concrete) and 5 mm (usual concrete). These estimations were based on measurements of the localization zone width on the concrete surface by means of the digital image correlation (DIC) technique (Skarżyński *et al.* 2011, Skarżyński and Tejchman 2010, 2013) and following comparative non-linear FE analyses with non-local softening. In our FE calculations of the composite slab we assumed l_c=5-20 mm. One calculation within elasto-plastic damage was also performed without regularization (l_c=0). Note that in order to obtain totally mesh-independent results within non-locality, the finite element size e should be smaller or equal to $e=3\times l_c$ (Tejchman and Bobinski 2012).

Reinforcement

In order to simulate the behaviour of the bottom and top reinforcement bars (modelled as one-dimensional truss elements), an elasto-perfect plastic constitutive law was assumed with E_s=200 GPa (modulus of elasticity) and $\sigma_y^s=f_y$=600 MPa (σ_y^s-yield steel stress).

In order to describe the interaction between concrete and reinforcement, a bond relationship was defined. In general, this relationship is complex and depends on several factors (e.g., concrete class, concrete cover, bar diameter, bar rib height and bar rib spacing). Two different bond-failure mechanisms may appear connected to a pull-out or splitting mode (Den Uijl and Bigaj 1996). It should be determined in the experiment with the same concrete and reinforcement. Several various reinforcement-concrete bond laws were proposed in the literature (Rehm and Eligehausen 1979, Eligehausen *et al.* 1982, Malvar 1992, Den Uijl and Bigaj 1996, Lowes *et al*. 2004 and Haskett *et al*. 2008). The effect of different bond-slip laws was investigated by Syroka-Korol *et al.* (2014). Our calculations were carried out with perfect bond and bond-slip. In the first case, the same displacements along a contact surface/line between concrete and reinforcement were assumed. Since the bond behaviour was not experimentally investigated, in the case of bond-slip, the analyses were carried out with a relationship between the bond shear stress τ_b and slip u using the simplest bond law by Dörr (1980) with 2 parameters only. It neglects softening and assumes a yield plateau

$$\begin{aligned} \tau_b &= f_t\left[0.5\left(\frac{u}{u_0}\right) - 4.5\left(\frac{u}{u_0}\right)^2 + 1.4\left(\frac{u}{u_0}\right)^3\right] \qquad && \text{if} \quad 0 < u \le u_0 \\ \tau_b &= 1.9 f_t && \text{if} \quad u > u_0 \end{aligned} \tag{8}$$

The parameter and u_0 is the displacement at which perfect slip occurs. In order to consider bond-slip, the interface with a zero thickness was assumed along a contact surface where the relationship between the shear traction and the slip was introduced. The assumed value of u_0 varied from 0 (perfect bond) up to 1 mm.

Expanded polystyrene

The EPS core was modelled as the elastic 3D elements with the modulus of elasticity E_{eps}=8.01 MPa and the Poisson's ratio ν_{eps}=0.25 based on own standard experiments (Smakosz and Tejchman 2014). During uniaxial compression, the initial part of the vertical stress-vertical strain diagram indicated a linear elastic behaviour at very low strain (up to 2%). Next the material underwent hardening connected to the densification. The densification was weak up to strain equal to ε=70% and later became very strong since the cellular foam structure was completely crushed. For the vertical normal strain of ε=10%, the

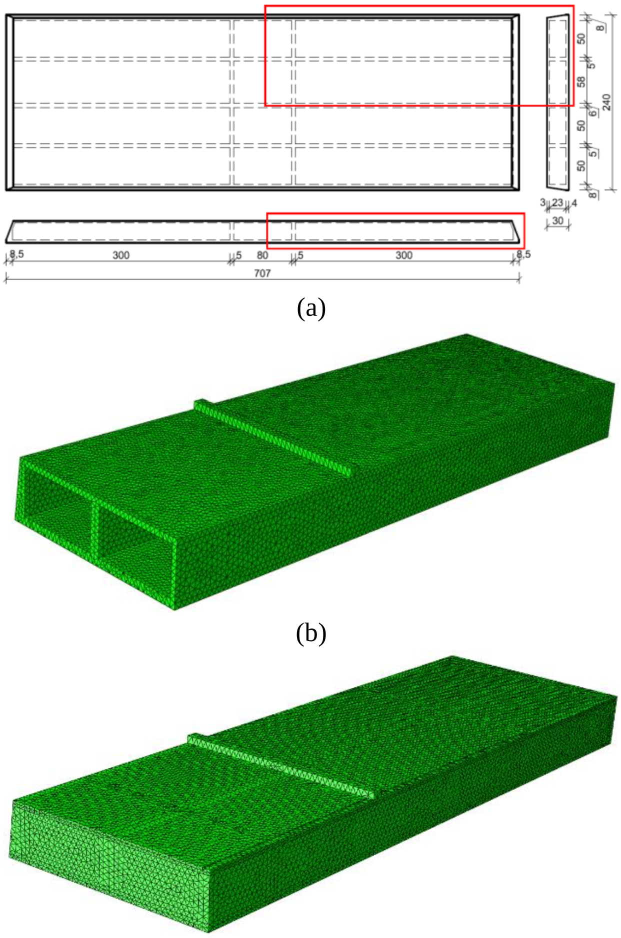

(a)

(b)

(c)

Fig. 11 Composite slab: (a) slab quarter assumed for FE calculations, (b) FE mesh without EPS and (c) FE mesh with EPS

vertical normal stress was σ_u=0.11 MPa (E=6.09 MPa, ν=0.25). During uniaxial tension, a brittle mode was observed due to the occurrence of a discrete tensile crack in the horizontal direction in the mid-region. Initially, the material behaviour was linear, later non-linear up to the peak. The maximum critical vertical normal stress was on average σ_u=0.22 MPa for ε=3.5% (E=10.37 MPa). The evolution of experimental curves from three-point bending tests and a failure mechanism were similar as in tension (the maximum vertical normal stress was on average σ_u=0.20MPa for ε=2.4% and E=8.01 MPa).

The two 3D enhanced models were implemented into the commercial finite element code Abaqus (2004) with the aid of the subroutine UMAT (user constitutive law definition) and UEL (user element definition) for efficient computations (Bobiński and Tejchman 2004). For the solution of the non-linear equation of motion governing the response of a system of finite elements, the initial stiffness method was used with a symmetric elastic global stiffness matrix (implicit approach). The calculations with the full Newton-Raphson method resulted in a poor convergence in a softening regime. In addition, the determination of a tangent stiffness matrix within a non-local plasticity is virtually impossible. The non-local averaging was

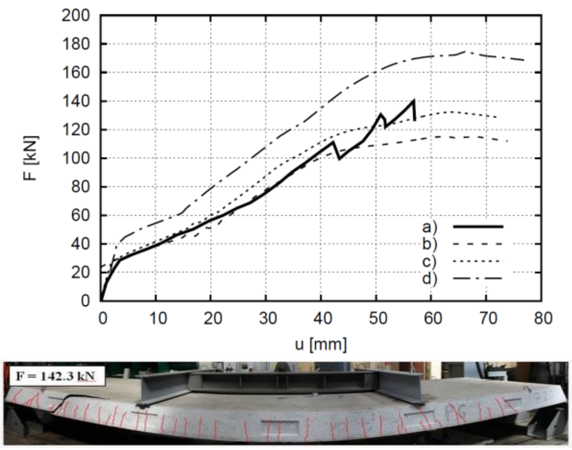

(a)

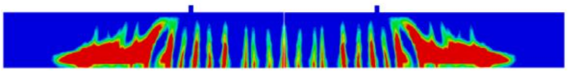

(b)

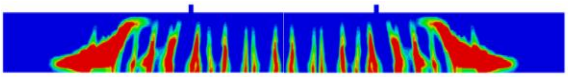

(c)

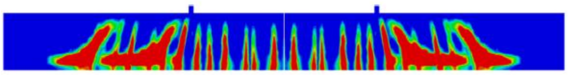

(d)

Fig. 12 Force-deflection curves and final distribution of non-local tensile softening parameter κ_2 (u=63 mm) for composite slab from FE analyses within enhanced elasto-plasticity with different tensile fracture energy G_f as compared to experiment of Fig. 4 (compressive fracture energy G_c=3250 N/m, characteristic length of micro-structure l_c=5 mm, perfect bond between steel and reinforcement): (a) experimental result at failure, (b) FEM with G_f=100 N/m (Fig. 9(Ca)), (c) FEM with G_f=200 N/m (Fig. 9(Cb)) and (d) FEM with G_f=400 N/m (Fig. 9(Cc))

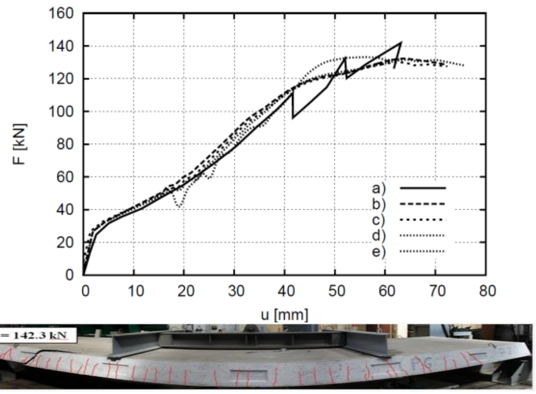

(a)

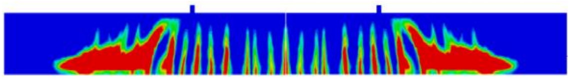

(b)

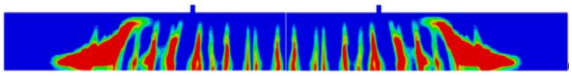

(c)

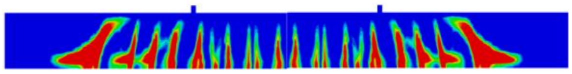

(d)

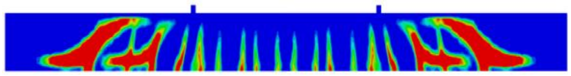

(e)

Fig. 13 Force-deflection curves and final distribution of non-local tensile softening parameter κ_2 (u=63 mm) for composite slab from FE analyses within enhanced elasto-plasticity as compared to experiment (compressive fracture energy G_c=3250 N/m, tensile fracture energy G_f=200 N/m and characteristic length of micro-structure l_c=5 mm): (a) experimental result at failure, (b) perfect bond, (c) bond-slip with u_0=0.03 mm, (d) bond-slip with u_0=0.06 mm and (e) bond-slip with u_0=1.0 mm (Eq. (8))

performed in the current configuration. This choice was governed by the fact that element areas in this configuration were automatically calculated by Abaqus (2004).

5. FE results for composite slab under bending

In the FE calculations, some simplifications were assumed. The slab part (1/4 of the entire slab) was analyzed only in order to strongly reduce the computation time (Fig.11). Thus, a symmetric failure mode was taken into account in contrast to the experimental results (Fig.6) and a statistical strength contribution of concrete was not considered. This contribution was namely very difficult to be estimated in view of an extremely strong non-symmetric failure mode in the experiments (usual statistical distributions of the tensile strength insignificantly affect the location of a diagonal shear crack, Korol *et al.* 2014). In addition, the initial bending cracks due to transportation were also not considered. Approximately 400,000 tetrahedral elements with linear shape functions were used: 200,000 for the RC slab and 200,000 for EPS. The element size was e=30 mm (i.e., e=6×l_c). The computation time was still very long, about 2 weeks using the computer Intel Xeon CPU 3.10 GHz (2 processors, 128 GB RAM, 64-bit system).

5.1 FE results within enhanced elasto-plasticity

Since the presence of the EPS foam increased the slab strength solely by 6% as compared to the FE calculations without the EPS core, the further computations were carried out without the EPS core. The compressive fracture energy of Fig. 9(B) did not affect both the force-deflection curve and distribution of the non-local softening parameter. Figure 12 shows the calculated load-deflection curves and localization zones in the composite slab for 3 different tensile fracture energies in tension of Fig. 9(C) (G_c=3250N/m, l_c=5 mm) and perfect bond between steel and reinforcement (without the slab weight). The calculated load-deflection curves and localization zones for the different initial bond-slip stiffness and perfect bond are in Fig. 13.

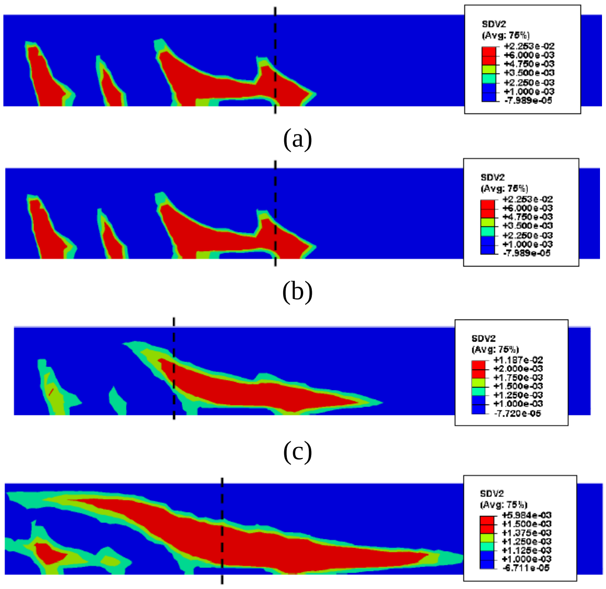
(a) (b) (c) (d)

Fig. 14 Distribution of non-local tensile softening parameter κ_2 on the right side of composite slab from FE analyses within enhanced elasto-plasticity for different vertical force values: (a) F=35 kN, (b) F=55 kN, (c) F=82 kN and (d) F_{max}=142.3 kN (failure) (tensile fracture energy G_f=200N/m, compressive fracture energy G_c=3250 N/m, bond-slip with u_0=0.03 mm and characteristic length of micro-structure l_c=5 mm)

Table 1 The comparison between experimental and theoretical results by Eq. (1)

Shear strength from experiments υ_{exp} (kPa)	Shear strength by Eq. (1) with different parameter υ_s υ (kPa)	Mean experimental distance of inclined crack from support $\bar{x}$ (m)	Theoretical distance of inclined crack from support x (m)
1316.43	1234.6 kPa (υ_s=0.67) 921.4 kPa (υ_s=0.50)	1.14	1.23

The vertical force increased with increasing tensile fracture energy G_f=100-400 N/m. For G_f=100 N/m, the calculated maximum vertical force $F_{\max}$ was smaller by 20% than the experimental one $F_{\max}$=142.3 kN (Fig. 12). However, for G_f=200 N/m, the calculated maximum vertical force $F_{\max}$ was smaller merely by 7% than the experimental one $F_{\max}$=142.3 kN (Fig. 12). In the case of G_f=400 N/m, the calculated was significantly too high (Fig.12). The calculated deflection for the maximum vertical force was 62.6 mm (Fig. 12(b)) and was similar to the experimental one (63 mm). The initial bond stiffness insignificantly influenced the force-deflection curve, however, it affected the distribution of the non-local tensile softening parameter (Fig. 13). The combined failure took place at the same place, both in the critical diagonal shear crack and along the bottom reinforcement (Fig. 14). There were vertical and inclined and long and short localization zones (Fig. 15). The width of vertical localization zones was about w_c=(3-4)×l_c whereas the width of the inclined localization zone was w_c=8×l_c. The calculated average spacing s of tensile localization zones using the model with G_c=3250 N/m, G_f=200 N/m and l_c=5 mm increased with decreasing initial bond stiffness from s_{lz}=150 mm for perfect bond, s_{lz}=155-160 mm for u_0=0.06 mm and s_{lz}=185mm for u_0=1.0 mm (the experimental average vertical crack spacing at failure was approximately 145mm, Fig. 5). The calculated distance of the critical diagonal

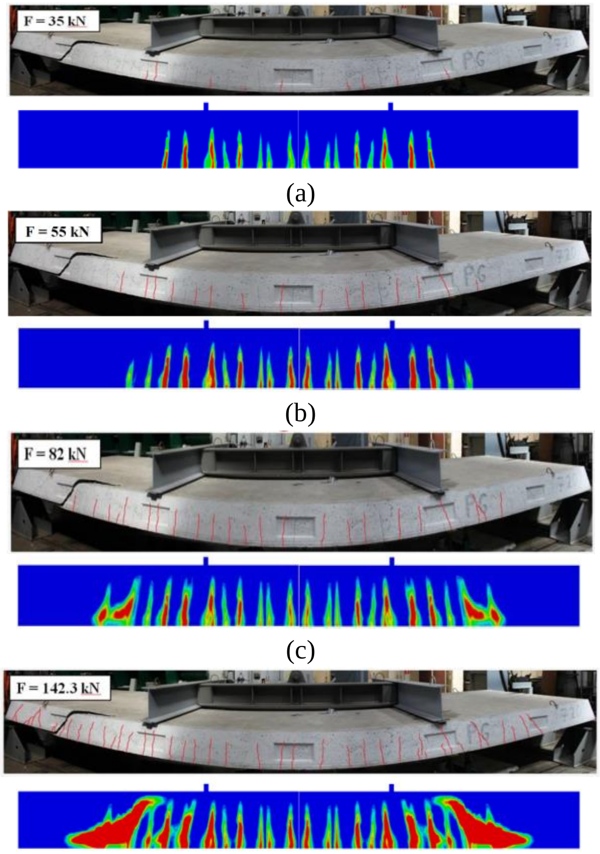

(a) (b) (c) (d)

Fig. 15 Comparison of calculated distribution of non-local tensile softening parameter κ_2 within enhanced elasto-plasticity in composite slab with experimental crack pattern for different vertical force values: (a) F=35 kN, (b) F=55kN, (c) F=82 kN and (d) F_{max}=142.3 kN (failure) (tensile fracture energy G_f=200 N/m, compressive fracture energy G_c=3250 N/m, bond-slip with u_0=0.03 mm and characteristic length of micro-structure l_c=5 mm)

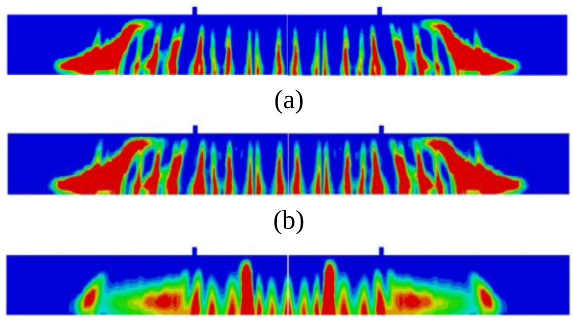
(a) (b) (c)

Fig. 16 Distribution of non-local tensile softening parameter κ_2 within enhanced elasto-plasticity in slab for maximum vertical force F_{max}=142.3 kN (tensile fracture energy G_f=200 N/m, compressive fracture energy G_c=3250 N/m) for different characteristic lengths: (a) l_c=5 mm, (b) l_c=10 mm and (c) l_c=20 mm

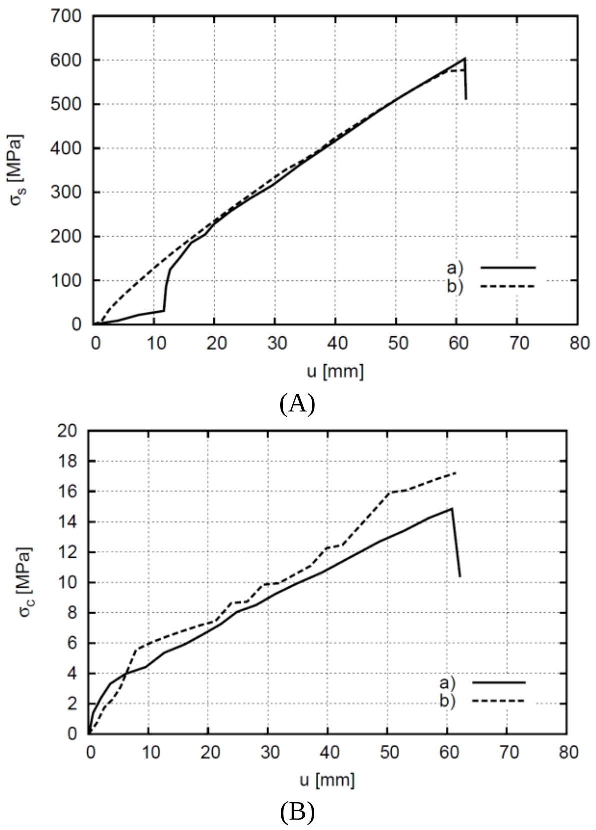

Fig. 17 Calculated and measured normal stress σ at slab mid-span versus deflection u: (A) tensile stress in bottom reinforcement, (B) compressive stress in concrete along slab top and (a) experiments and (b) FE results within enhanced elasto-plasticity

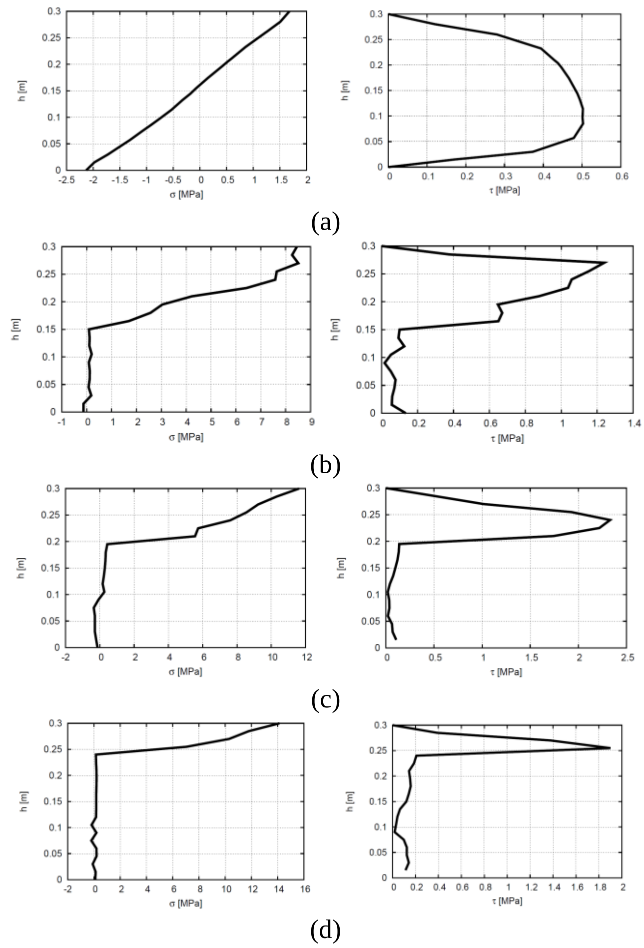

Fig. 18 Distribution of normal σ and shear stress τ along slab thickness h in vertical cross-sections (vertical dashed lines in Fig. 14) for different loading stages (results within elasto-plasticity with non-local softening)

shear localization zone from the support was strongly affected by the bond stiffness; it was at the distance of x=1.48 m for perfect bond, x=1.20 m for u_0=0.03 mm, x=1.07 m for u_0=0.06 mm and x=0.96 m for u_0=1.0 mm from the support (Fig. 13) along the slab bottom line (against $\bar{x}$ =1.14 cm in the experiment, Table 1). The mean length of calculated bending vertical localization zones, l_{lc}=0.20 m (Fig. 15), was similar as in experiments (0.19 m). The best agreement with experiments was obtained for the following material parameters: G_c=3250 N/m, G_f=100-200N/m, u_0=0-0.06mm and characteristic length l_c=5 mm. The effect of l_c=5-10mm on the pattern of localization zones was negligible (Fig. 16). The calculated inclination of the critical shear zone with respect to the bottom edge was θ=38.6º and was smaller by 7º than the mean experimental value of θ=45.5º.

For the force F=35 kN, more vertical localization zones were calculated (s_{lz}=240 mm) (Fig. 15) than cracks in the experiment (s_c=350 mm). For F=55 kN, the calculated spacing of localization zones was s_{lz}=200 mm (s_c=200 mm), for F=82 kN-s_{lz}=182 mm (s_c=170 mm) and for F_{max}=142.3 kN-s_{lz}=155 mm (s_c=145 mm). The calculated critical diagonal shear localization zone was at the distance of x=1.20 m (for u=0.03 mm) from the support (against $\bar{x}$ =1.14 m in the experiment).

Fig. 17 shows the comparison of numerical and experimental normal stresses in tensile reinforcement and compressive concrete at the mid-span. The calculated maximum normal tensile stress in reinforcement at failure was 578 MPa (in the experiment 614 MPa) (Fig. 17(a)). The calculated maximum compressive stress in concrete in FEM was at failure 17.2 MPa whereas in the experiment it was 14.5 MPa (Fig. 17(b)). The maximum normal stress in expanded polystyrene was 0.15 MPa (<σ_u=0.20 MPa) and was measured in the neighbourhood of the transverse rib at the end of the loading process. Thus, the assumption of a linear elastic behaviour of EPS was correct. The normal and

Table 2 FE results versus experimental outcomes

Result	Enhanced elasto-plasticity	Enahanced elasto-plastic-damage	Experiment
Maximum vertical force F_{max} (kN)	129.7	133.6	142.3
Spacing of vertical cracks (localization zones) at failure load s (mm)	155	125	145
Mean location of critical diagonal shear crack (localization zone) from support x (m)	1.20	1.27	1.14
Mean inclination of critical diagonal shear crack (localization zone) θ (º)	38.6º	42.5º	45.5º

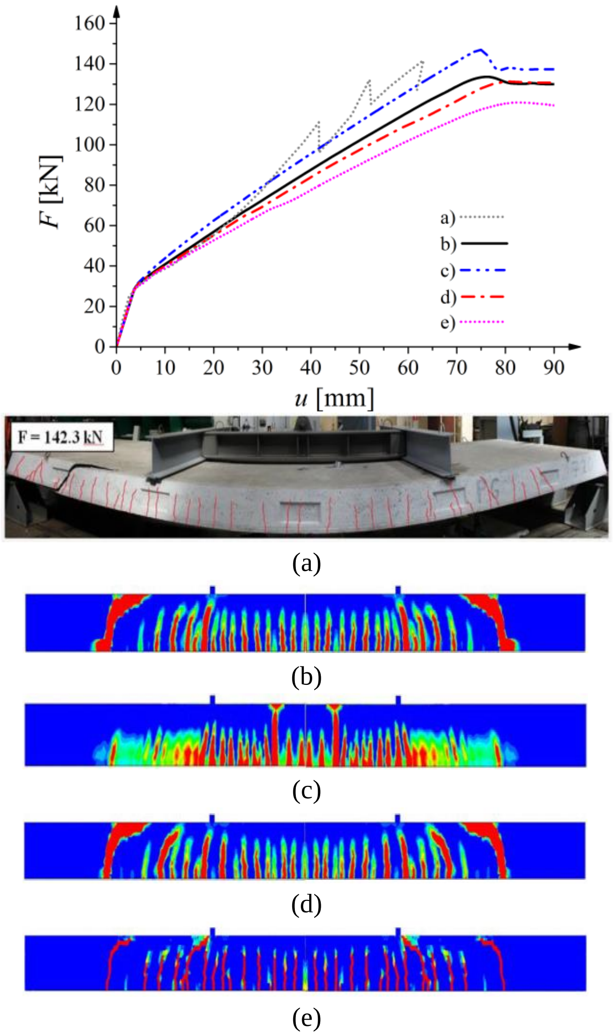

Fig. 19 Force-deflection curves and distribution of non-local equivalent strain measure (u=70 mm) for composite slab from FE analyses within enhanced coupled elasto-plastic-damage and bond-slip law as compared to experiment (characteristic length of micro-structure l_c=5mm): (a) experimental result, (b) FE result with set of material constants in Section 4, (c) FE result with tensile hardening modulus H_p=7.5 GPa (instead of 19 GPa), (d) FE result with softening constant β=300 (instead of 100) and (e) FE result with characteristic length l_c=0 mm (instead of l_c=5 mm)

shear stress distribution along the slab thickness in vertical cross-sections are presented in Fig. 18. At the failure, the normal and shear stress along the crack were almost equal to 0. Above the crack, the maximum normal stress was 12MPa and maximum shear stress 2.2 MPa (Fig. 18(d)).

5.2 FE results within enhanced coupled elasto-plastic-damage

The results for coupled elasto-plastic-damage model with the bond-slip law (u_0=0.03 mm) are described in Figs. 19 and 20. In addition, the comparative calculations were carried out without regularization (l_c=0 mm) (Fig. 19(e)). The calculated mean ultimate vertical force differed by

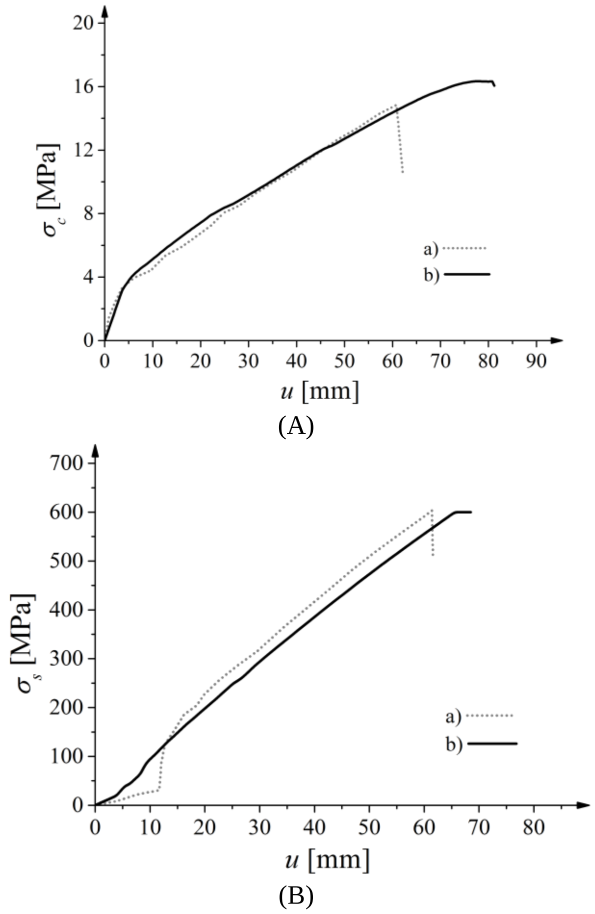

Fig. 20 Calculated and measured normal stress σ at slab mid-span versus deflection u: (A) tensile stress in bottom reinforcement, (B) compressive stress in concrete along slab top, (a) experiments and (b) FE result within enhanced coupled elasto-plastic-damage

about 3-10% from the experimental force with l_c=5 mm and by 20% with l_c=0 mm. The best agreement was achieved with H_p=19 GPa (~0.6E_c), β=100 and l_c=5 mm; the difference was merely 3% (curve '*b*' in Fig. 19). The maximum vertical force slightly became larger with decreasing hardening plastic modulus H_p in tension, increasing l_c and decreasing softening parameter β corresponding to the larger tensile fracture energy (Fig. 19). The influence of H_p on $F_{\max}$ was more pronounced than of β. For H_p=19 GPa the failure mechanism was solely governed by the growth of a critical diagonal shear crack (the bond did not fail as in the elasto-plastic approach) (Figs. 19(b), 19(d) and 19(e)). The decrease of both the softening parameter β and characteristic length l_c insignificantly influenced the crack pattern and the position of the critical diagonal crack. In turn, a decrease of the plastic modulus H_p caused a different failure mechanism through bending (Fig. 19(c)) due to a smaller increase of the elastic strain and consequently to the smaller equivalent strain which was defined in terms of elastic strains. A similar effect was observed within the enhanced elasto-plasticity with very large fracture energy (Fig. 16(c)). For l_c=5 mm, the width of the short vertical localization zones was w_c=(3-4)×l_c and of the long vertical and inclined cracks was w_c=(6-8)×l_c. In the case of l_c=0 mm, the width of localization zones was limited to the element size. The calculated average spacing of localization zones varied for l_c=5 mm between s_{lz}=125 mm for all zones and s_{lz}=155 mm for the long localization zones in view of the experimental crack spacing s_c=145 mm. In the case of l_c=0 mm, the average distance of localization zones was s_{lz}=125 mm (all zones) and s_{lz}=165 mm (long zones only). The calculated length of localization zones due to bending was 11-26 mm (l_c=0-5 mm). In the case of l_c=0 mm, an additional inclined localization zone was obtained under loading points (Fig.19(e)) in contrast to experiments. The critical diagonal shear localization zone was created for x=127 cm (138 cm for perfect-bond) from the support (in the experiment $\bar{x}$ =114 cm). Its inclination to the horizontal line was θ=42.5º<$\bar{\theta}$ =45.5º (l_c=5 mm) and θ=46º (l_c=0 mm). The calculated maximum von Mises stress in tensile reinforcement at the mid-span was 600 MPa, whereas in the experiment 614 MPa (Fig. 20(b)). The calculated maximum compressive stress in concrete at failure at the mid-span was 16.2 MPa, whereas in the experiment 14.5 MPa (Fig.20(a)).

Summarizing, both the enhanced constitutive continuum models for concrete satisfactorily captured the slab behaviour under 4-point bending. Good accordance between the numerical and experimental outcomes was achieved with respect to the maximum vertical force, failure mode, location of the critical inclined localization zone (both models) and localization zone spacing (enhanced elasto-plasticity) (Table 2). The bond-slip stiffness significantly influenced the location of the critical diagonal shear crack. The differences between experiments and calculations were probably caused by the fact that: a) a symmetric failure mode was taken into account in the FE calculations, b) the FE mesh size assumed was still too large, 6×l_c, instead of the recommended one e≤(2-3)×l_c and c) the material imperfections were not considered which strongly influenced the non-uniform slab behaviour at the failure.

6. Conclusions

Based on the experimental and numerical investigations of novel composite building slabs subjected to four-point bending in the scale 1:1, a number of conclusions can be drawn in the following:

• The EPS foam negligibly influenced the force-deflection curve and crack pattern.

• The experimental slab failure was brittle and characterized by the occurrence of a diagonal shear crack. The diagonal failure crack was strongly non-symmetric along the slab width. Its inclination to the horizontal varied between 38º and 53º. It occurred 1.14 m on average from the slab support. The mean experimental spacing of main vertical cracks was smaller than this according to Eq. (4), smaller by 15% than this according to Eq. (3) and smaller by 70% than this according to Eq. (2). It was recommended to slightly increase the horizontal longitudinal reinforcement area bars in order to decrease the slab deflection and to connect the bottom slab with longitudinal ribs in order to increase the shear capacity.

• Both the enhanced constitutive continuum models for concrete satisfactorily captured the behaviour of the slab under 4-point bending although the slab quarter, twice too large finite elements and no material imperfections were used. The good accordance between the numerical and experimental outcomes was achieved with respect to the failure mode, shear strength, deflection and location of the critical diagonal localization shear zone. The differences between the models mainly concerned the spacing and pattern of localization zones and inclination of the failure diagonal shear crack. A coupled elasto-plastic-damage model with non-local softening is recommended for calculations due its more physical foundations when describing a non-linear behaviour of concrete under tension.

• The shear capacity slightly increased with increasing tensile fracture energy and decreasing hardening plastic modulus in tension.

• The calculated average spacing s_{lz} of bending localization zones varied between 96-148 mm and decreased with decreasing bond stiffness. For the perfect bond or bond-slip with the small slip parameter within the range u_0=0-0.06 mm using the simple bond-slip law by Dörr (1980), it was similar to the average experimental crack spacing of 145 mm. The mean height of calculated localization zones was close to the experiments.

• The computed distance of the critical shear localization zone from the support decreased with decreasing bond stiffness (from 1.48 m down to 0.96 m). With the bond-slip displacement of u_0=0.03 mm, it was close to the mean experimental value of 114 cm.

• The experimental shear strength was realistically described with the analytical formula for RC beams without shear reinforcement (Eq. (1)) by assuming the sliding reduction factor υ_s=0.67. However, the inclination of the critical diagonal shear crack to the horizontal was significantly higher in experiments than the theoretical solution.

Acknowledgments

Research work has been carried out within the project: “Innovative complex system solution for energy-saving residential buildings of a high comfort class in an unique prefabricated technology and assembly of composite panels” financed by the National Centre of Research and Development NCBR (NR. R1/INNOTECH-K1/IN1/59/155026/NCBR/12).

The FE simulations were performed on computers of the Academic Computer Centre in Gdańsk TASK.

References

Abaqus (2004), *Theory Manual, Version 5.8*, Hibbit, Karlsson & Sorensen Inc.

Bažant, Z.P. and Jirasek, M. (2002), “Non-local integral formulations of plasticity and damage: Survey of progress”, *J. Eng. Mech.*, **128**(11), 1119-1149.

Bažant, Z.P., Le, J.L. and Hoover, C. (2010), "Nonlocal boundary layer model: overcoming boundary condition problems in strength statistics and fracture anslysis of quasibrittle materials", *Proceedings of the Fracture Mechanics of Concrete and Concrete Structures*, Jeju Island, Korea.

Bobiński, J. and Tejchman J. (2004), "Numerical simulations of localization of deformation in quasi-brittle materials within non-local softening plasticity", *Comput. Concrete*, **1**(4), 1-22.

Borino, G., Failla, B. and Parrinello, F. (2003), "A symmetric nonlocal damage theory", *J. Sol. Struct.*, **40**(13), 3621-3645.

Brinkgreve, R.B.J. (1994), "Geomaterial models and numerical analysis of softening", Ph.D. Dissertation, Delft University of Technology, the Netherlands.

Carol, I. and Willam, K. (1996), "Spurious energy dissipation/generation in stiffness recovery models for elastic degradation and damage", *J. Sol. Struct.*, **33**(20-22), 2939-2957.

CEB-FIP Model Code (1990), *Concrete Structures*, **228**, 1-205.

Chen, J.F., Morozov, E.V. and Shankar, K. (2012), "A combined elastoplastic damage model for progressive failure analysis of composite materials and structures", *Compos. Struct.*, **94**(12), 3478-3489.

De Luca, A., Zadeh, H. and Nanni, A. (2014), "In situ load testing of a one-way reinforced concrete slab per the ACI 437 standard", *J. Perform. Constr. Facil.*, **28**(5), 04014022.

Den Uijl, J.A. and Bigaj, A.J. (1996), "A bond model for ribbed bars based on concrete confinement", *Heron*, **41**(3), 201-226.

Dörr, K. (1980), "Ein beitag zur berechnung von stahlbetonscheiben unter berücksichtigung des verbundverhaltens", Ph.D. Dissertation, Darmstadt University.

Dulude, C., Ahmed, E., El-Gamal, S. and Benmokrane, B. (2011), "Testing of large-scale two-way concrete slabs reinforced with GFRP Bars", *Proceedings of the 5th International Conference on FRP Composites in Civil Engineering*, Beijing, China, September.

Eligehausen, R., Popov, E.P. and Bereto, V.V. (1982), "Local bond stress-slip relationships of deformed bars under generalized excitations", *Proceedings of the 7th European Conference on Earthquake Engineering*, Athens.

Etse, G. and Willam, K. (1994), "Fracture energy formulation for inelastic behavior of plain concrete", *J. Eng. Mech.*, **120**(9), 1983-2011.

Eurocode 2: PN-EN (1992), *Design of Concrete Structures-Part 1: General Rules and Rules for Buildings*.

Faria, R., Oliver, J. and Cervera, M. (1998), "A strain-based plastic viscous-damage model for massive concrete structures", *J. Sol. Struct.*, **35**(14), 1533-1558.

Feenstra, P.H. and De Borst, R. (1996), "A composite plasticity model for concrete", *J. Sol. Struct.*, **33**(5), 707-730.

Gabet, T., Malecot, Y. and Daudeville, L. (2008), "Triaxial behaviour of concrete under high stresses: Influence of the loading path on compaction and limit states", *Cement Concrete Res.*, **38**(3), 403-412.

Geers, M.G.D. (1997), "Experimental analysis and computational modeling of damage and fracture", Ph.D. Dissertation, Eindhoven University of Technology, Eindhoven, the Netherlands.

Giry, C., Dufour, F. and Mazars, J. (2011), "Stress-based nonlocal damage model", *J. Sol. Struct.*, **48**(25), 3431-3443.

Grassl, P., Xenos, D., Nyström, U., Rempling, R. and Gylltoft, K. (2013), "CDPM2: A damage-plasticity approach to modelling the failure of concrete", *J. Sol. Struct.*, **50**, 3805-3816.

Haskett, M., Pehlers, D.J. and Mohamed Ali, M.S. (2008), "Local and global bond characteristics of steel reinforcing bars", *Eng. Struct.*, **30**(2), 376-383.

Korol, E. Tejchman, J. and Mróz, Z. (2014), "FE analysis of size effects in reinforced concrete beams without shear reinforcement based on stochastic elasto-plasticity with non-local softening", *Fin. Elem. Analy. Des.*, **88**, 25-41.

Korol, E. Tejchman, J. and Mróz, Z. (2017), "Experimental and numerical assessment of size effect in geometrically similar slender concrete beams with basalt reinforcement", *Eng. Struct.*, **141**, 272-291.

Krajcinovic, D. and Fonseka, G. (1981), "The continuous damage theory of brittle materials", *J. Appl. Mech.*, **48**(4), 809-824.

Lantsoght, E., Van Der Veen, C. and Walraven, J. (2010), "Shear tests of reinforced concrete slabs with concentrated loads near to supports", *Proceedings of the 8th FIB Ph.D. Symposium in Kgs. Lyngby*, Denmark.

Lee, J. and Fenves, G.L. (1998), "Plastic-damage model for cyclic loading of concrete structures", *J. Eng. Mech.*, **124**(8), 892-900.

Lorrain, M., Maurel, O. and Seffo, M. (1998), "Cracking behaviour of reinforced high-strength concrete tension ties", *ACI Struct. J.*, **95**(5), 626-635.

Lowes, L.N., Moehle, J.P. and Govindjee, S. (2004), "Concrete-steel bond model for use in finite element modeling of reinforced concrete structures", *ACI Struct. J.*, **101**(4), 501-511.

Lubliner, J., Oliver, J., Oller, S. and Onate, E. (1989), "A plastic-damage model for concrete", *J. Sol. Struct.*, **25**(3), 299-326.

Mahnken, R. and Kuhl, E. (1999), "Parameter identification of gradient enhanced damage models", *Eur. J. Mech. A/Sol.*, **18**(5), 819-835.

Majewski, T., Bobinski, J. and Tejchman, J. (2008), "FE-analysis of failure behaviour of reinforced concrete columns under eccentric compression", *Eng. Struct.*, **30**(2), 300-317.

Malvar, L.J. (1992), "Bond reinforcement under controlled confinement", *ACI Mater. J.*, **96**(6), 593-601.

Marzec, I. and Tejchman, J. (2012), "Enhanced coupled elasto-plastic-damage models to describe concrete behaviour in cyclic laboratory tests: Comparison and improvement", *Arch. Mech.*, **64**(3), 227-259.

Marzec, I., Bobinski, J. and Tejchman, J. (2007), "Simulations of crack spacing in reinforced concrete beams using elastic-plasticity and damage with non-local softening", *Comput. Concrete*, **4**(5), 377-403.

Marzec, I., Skarżyński, Ł., Bobiński, J. and Tejchman, J. (2013), "Modelling reinforced concrete beams under mixed shear-tension failure with different continuous FE approaches", *Comput. Concrete*, **12**(5), 585-612.

Mazars, J. (1986), "A description of micro- and macroscale damage of concrete structures", *Eng. Fract. Mech.*, **25**(5-6), 729-737.

Mihai, I.C., Jefferson, A.D. and Lyons, P. (2016), "A plastic-damage constitutive model for the finite element analysis of fibre reinforced concrete", *Eng. Fract. Mech.*, **159**, 35-62.

Nielsen, M.P. and Bræstrup, M. (1976), *W. Plastic Shear Strength of Reinforced Concrete Beams*, Report R 73, University of Denmark.

Pamin, J. and De Borst, R. (1999), "Stiffness degradation in gradient-dependent coupled damage-plasticity", *Arch. Mech.*, **51**(3-4), 419-446.

Peerlings, R.H.J., De Borst, R., Brekelmans, W.A.M. and Geers, M.G.D. (1998), "Gradient enhanced damage modelling of concrete fracture", *Mech. Cohes.-Frict. Mater.*, **3**(4), 323-342.

Pijauder-Cabot, G. and Bažant, Z.P. (1987), "Non-local damage theory", *ASCE J. Eng. Mech.*, **113**, 1512-1533.

Pijauder-Cabot, G. and Dufour, F. (2010), "Non-local damage model boundary and evolving boundary effects", *Eur. J. Environ. Civil Eng.*, **14**(6-7), 729-749.

Polish Standard (2002), PN-B-03264.

Polizzotto, C, Borino, G. and Fuschi, P. (1998), "A thermodynamically consistent formulation of nonlocal and gradient plasticity", *Mech. Res. Commun.*, **25**(1), 75-82.

Rehm, G. and Eligehausen R. (1979), "Bond of ribbed bars under high cycle repeated loads", *J. Am. Concrete Inst.*, 297-309.

Saouridis, C. and Mazars, J. (1992), "Prediction of the failure and size effect in concrete via a bi-scale damage approach", *Eng. Comput.*, **9**(3), 329-344.

Sewaco System, Patent Implementations, PCT/PL2012/000076, P.396140, P.400541, P.400558.

Simo, J.C. and Ju, J. (1987), "Strain- and stress-based continuum damage models-I. Formulation", *J. Sol. Struct.*, **23**(7), 821-840.

Skarżyński, Ł, Syroka, E. and Tejchman, J. (2011), "Measurements and calculations of the width of fracture process zones on the surface of notched concrete beams", *Strain*, **47**(s1), 319-332.

Skarżyński, Ł. and Tejchman, J. (2010), "Calculations of fracture process zones on meso-scale in notched concrete beams subjected to three-point bending", *Eur. J. Mech./A Sol.*, **29**(4), 746-760.

Skarżyński, Ł. and Tejchman, J. (2013), "Experimental investigations of fracture process in plain and reinforced concrete beams under bending", *Strain*, **49**(6), 521-543.

Smakosz, Ł. and Tejchman, J. (2014), "Evaluation of strength, deformability and failure mode of composite structural insulated panels", *Mater. Des.*, **54**, 1068-1082.

Syroka-Korol, E. and Tejchman, J. (2014), "Experimental investigations of size effect in reinforced concrete beams failing by shear", *Eng. Struct.*, **58**, 63-78.

Tejchman, J. and Bobiński, J. (2012), *Continuous and Discontinuous Modeling of Fracture in Concrete Using FEM*, Springer, Berlin-Heidelberg.

Website: www.sewaco.pl.

Willam, K.J. and Warnke, E.P. (1975), "Constitutive model for the triaxial behavior of concrete", *Proceedings of the Concrete Structures Subjected to Triaxial Stresses*, Begamo, Italy.

Xotta, G., Beizaee, S. and Willam, K.J. (2016), "Bifurcation investigations of coupled damage-plasticity models for concrete materials", *Comput. Meth. Appl. Mech. Eng.*, **298**, 428-452.

Zhang, J.P. (1994), *Strength of Cracked Concrete. Part 1: Shear Strength of Conventional Reinforced Concrete Beams, Deep Beams, Corbels and Prestressed Reinforced Concrete Beams without Shear Reinforcement*, Report of Technical University of Denmark, Lungby Denmark.

CC

Appendix 1

In order to describe the concrete behaviour by an elasto-plastic constitutive model, two failure criteria were assumed. In the tensile regime, the Rankine criterion was used with the yield function f_1 using isotropic softening and associated flow rule and in the compressive regime, the Drucker-Prager yield surface f_2 with isotropic hardening/softening and non-associated flow rule was used

$$f_1(\sigma_i, \kappa_1) = \max\{\sigma_1, \sigma_2, \sigma_3\} - \sigma_t(\kappa_1) \le 0, \quad \text{(A1)}$$

$$f_2(\sigma_{ij}, \kappa_2) = q - p \times tan\varphi - c(\kappa_2) = q - p \times tan\varphi - \left(1 - \frac{1}{3}tan\varphi\right)\sigma_c(\kappa_2) \le 0 \quad \text{(A2)}$$

$$q = \sqrt{\frac{3}{2}s_{ij}s_{ij}}\,,\ p = -\frac{1}{3}\sigma_{kk} \quad \text{(A3)}$$

$$\tan\varphi = \frac{3\left(1 - r_{bc}^{\sigma}\right)}{1 - 2r_{bc}^{\sigma}}, \quad \text{(A4)}$$

$$g_1 = f_1, \quad \text{(A5)}$$

$$g_2 = q - p\tan\psi, \quad \text{(A6)}$$

where: σ_i-principal stresses (i=1, 2, 3), σ_t-uniaxial tensile yield stress, κ_1-softening parameter equal to the maximum principal plastic strain ε_1^p, q-Mises equivalent deviatoric stress, p-mean stress, φ-the internal friction angle in the meridional stress plane (p–q plane), c-cohesion related to uniaxial compression strength, s_{ij}-the deviator of the stress tensor σ_{ij}, ($s_{ij}=\sigma_{ij}+\delta_{ij}p$) σ_c-uniaxial compression yield stress, κ_2-the hardening/softening parameter corresponding to the vertical normal plastic strain during uniaxial compression, g_i-flow potential function, r_{bc}^{σ}-the ratio between the biaxial compressive strength and uniaxial compressive strength ($r_{bc}^{\sigma}\approx 1.2$) and ψ-the dilatancy angle ($\psi\neq\varphi$). The last term in Eq. (A2) results from the yield condition q-$p\times\tan\varphi$-c=0 for uniaxial compression with $q=\sigma_c$ and $p=1/3\sigma_c$.

Appendix 2

The coupled elasto-plastic-damage model for concrete (Marzec and Tejchman 2012, Marzec *et al.* 2013) combines elasto-plasticity with a scalar isotropic damage (Simo and Ju 1987) assuming a strain equivalence hypothesis according to Pamin and de Borst (1999). The elasto-plasticity was defined in terms of effective stresses according to

$$\sigma_{ij}^{eff} = C_{ijkl}^{e}\varepsilon_{kl}\,. \quad \text{(A7)}$$

In an elasto-plastic regime, a linear isotropic Drucker-Prager criterion with a non-associated flow rule in compression and a Rankine criterion with an associated flow rule in tension (Appendix 1) defined by the effective stresses were used. The material degradation was calculated within isotropic damage mechanics, independently in tension and compression using one equivalent strain measure $\tilde{\varepsilon}$ by Mazars (1986) (ε_i-principal strains).

$$\tilde{\varepsilon} = \sqrt{\sum_i \langle \varepsilon_i \rangle^2}, \quad \text{(A8)}$$

The equivalent strain measure $\tilde{\varepsilon}$ was defined in terms of elastic strains. The stress-strain relationship was represented by the following formula

$$\sigma_{ij} = (1 - D)\sigma_{ij}^{eff} \quad \text{(A9)}$$

with the term '1-D' defined as

$$(1 - D) = (1 - s_c D_t)(1 - s_t D_c), \quad \text{(A10)}$$

wherein

$$D_t = 1 - \frac{\kappa_0}{\kappa}(1 - \alpha + \alpha e^{-\beta(\kappa - \kappa_0)}), \quad \text{(A11)}$$

$$D_c = 1 - \left(1 - \frac{\kappa_0}{\kappa}\right)\left(0.01\frac{\kappa_0}{\kappa}\right)^{\eta_1} - \left(\frac{\kappa_0}{\kappa}\right)^{\eta_2} e^{-\delta(\kappa - \kappa_0)}, \quad \text{(A12)}$$

$$s_t = 1 - a_t w\left(\sigma_{ij}^{eff}\right) \text{ and } s_c = 1 - a_c\left(1 - w\left(\sigma_{ij}^{eff}\right)\right), \quad \text{(A13)}$$

$$w\left(\sigma_{ij}^{eff}\right) = \begin{cases} 0 & \text{if } \sigma_{ij}^{eff} = 0 \\ \dfrac{\sum\langle \sigma_i^{eff} \rangle}{\sum\left|\sigma_i^{eff}\right|} & \text{otherwise} \end{cases}, \quad \text{(A14)}$$

where D_t and D_c are the damage parameters which describe the damage evolution under tension (Peerlings *et al.* 1998) and compression (Geers 1997 with the material constants: α, β, η_1, η_2 and δ. The splitting factors are a_t and a_c and $w\left(\sigma_{ij}^{eff}\right)$ denotes the stress weight function (Lee and Fenves 1998). The Macauley bracket in Eq. (A14) is defined as $\langle x \rangle = (x + |x|)/2$. All material constants are summarized in Table 3.

Table 3 Summary of material constants in coupled elasto-plastic-damage model

Parameter	Descritpion
Elastic behaviour	
E	- Young modulus
υ	- Poisson's ratio
Plastic behaviour	
ψ, φ	- dilatancy and internal friction angle
σ_{yt}^0, σ_{yc}^0	- initial yield stress under tension and ompression
H_p	- hardening modulus
Damage behaviour	
κ_0	- threshold parameter when damage starts
α, β	- parameters of softening tensile function
η_1, η_2, δ	- parameters of softening compressive function
a_t, a_c	- splitting factors (influence damage magnitude in tension and compression)